Significant suppression of two-magnon scattering in ultrathin Co by controlling the surface magnetic anisotropy at the Co/nonmagnet interfaces

Shugo Yoshii, Keisuke Kato, Ei Shigematsu, Ryo Ohshima, Yuichiro Ando, Koji Usami, and Masashi Shiraishi

Phys. Rev. B **106**, 174414 — Published 16 November 2022

DOI: 10.1103/PhysRevB.106.174414

Significant suppression of two-magnon scattering in ultrathin Co by controlling the surface magnetic anisotropy at the Co/nonmagnet interfaces

Shugo Yoshii[1], Keisuke Kato[2], Ei Shigemastu[1], Ryo Ohshima[1], Yuichiro Ando[1], Koji Usami[2], and Masashi Shiraishi[1, †]

[1]Department of Electronic Science and Engineering, Kyoto University, Nishikyo-ku, Kyoto 615-8510, Japan

[2]Research Center for Advanced Science and Technology, The University of Tokyo, Meguro-ku, Tokyo 153-8904, Japan

[†]Masashi Shiraishi (author to whom correspondence should be addressed). E-mail address: shiraishi.masashi.4w@kyoto-u.ac.jp

Abstract

To enable suppression of two-magnon scattering (TMS) in nanometer-thick Co (ultrathin Co) layers and realize low magnon damping in such layers, the magnon damping in ultrathin Co layers grown on various nonmagnetic seed layers with different surface magnetic anisotropy (SMA) energies are investigated. We verify the significantly weak magnon damping realized by varying the seeding layer species used. Although TMS is enhanced in ultrathin Co on Cu and Al seeding layers, insertion of Ti seeding layer below the ultrathin Co greatly suppresses the TMS, which is attributed to suppression of the SMA at the interface between Co and Ti. The Gilbert damping constant of the ultrathin Co layer on Ti (3 nm), 0.020, is comparable to the value for bulk Co, although the Co layer thickness here is only 2 nm. Realization of such weak magnon damping can open the door to tunable magnon excitation, thus enabling coupling of magnons with other quanta such as photons, given that the magnetization of ultrathin ferromagnets can be tuned using an external electric field.

I. Introduction

The magnon, which is a quasi-particle form of a spin wave and represents the minimum excitation state of the ferromagnetic ground state, is expected to be used as an information carrier with low energy consumption because of its long lifetime [1,2]. Magnons can couple with other quanta and quasiparticles, e.g., photons and phonons, respectively, and the interplay between the coupling strengths and relaxation rates of the magnons and the coupled media enables exploration of novel quantum technologies. In fact, when the coupling strength is greater than the relaxation rates of both the magnon and the coupled medium, a strong coupling state can be created that allows superposition of quantum states between the two quantum systems, i.e., between magnons and photons [3–5]. Because of the considerable attractiveness of this strong coupling state, which allows quantum computation [6–8], quantum sensing [9–11], and novel spintronic functions [12,13] to be realized, the coupling of magnons and photons has been drawing tremendous research attention in recent decades. When the great potential for use of strong magnon-photon coupling in quantum computation and novel spintronics is considered, a capability for reversible and versatile tuning of the coupling strength from weak to strong becomes quite significant. However, the current obstacle to the application of magnon-photon coupling is low tunability. Indeed, there are some studies aiming to realize tunable magnon-photon coupling via modulation of photon excitation [14,15]. However, to note is that direct control of a magnon state was demonstrated only via temperature control, where tuning of the coupling between magnons excited in gadolinium-iron-garnet (GIG) and photons confined within a three-dimensional microwave cavity was realized [16]. Although the realization of tunable magnon-photon coupling was quite noticeable, it is not easy to envisage practical applications of these temperature-controlled coupling states in either quantum technologies or spintronics. Therefore, subsequent studies to explore the novel processes required to realize tunable coupling states have been long awaited.

The recent discovery of gate-tunable magnetization in ultrathin Co [17,18] and in a few atomic layers of Fe [19] in addition to gate-tunable spin-orbit interaction (SOI) observations in ultrathin Pt and Pd layers [20–22] enabled exploration of new horizons in nano-spintronics, because these studies countered previous understandings in the research field that the magnetization of ferromagnetic materials cannot be controlled using an electric field and that the magnitude of the SOI in solids is material-specific. Given that application of a strong electric field enables dense carrier accumulation in ultrathin solids that also yields efficient modulation of their Fermi levels, successful modulation of the Fermi level of an ultrathin ferromagnetic film [17–19] can pave the way toward realization of magnetic anisotropy modulation, which would result in modulation of the magnon excitation. Therefore, magnon excitation in ultrathin ferromagnets represents the first milestone in the route towards achieving gate-tunable magnon-photon coupled systems. Although the linewidth of the ferromagnetic resonance (FMR) of ultrathin ferromagnets, which provides a good index of the magnon excitation, was too large (ca. 200 mT [23]), insertion of a Ta seeding layer beneath the 1-nm-thick Co layer produced a prominent FMR spectrum with a linewidth of 15 mT [24], which represents the first demonstration of salient magnon excitation in ultrathin ferromagnets. However, it should be also noted that the Gilbert damping constant α of the Co (1 nm)/Ta (3 nm) system is not sufficiently small, and considerable effort is still required to suppress α. Because α consists in principle of three components, i.e., the intrinsic, spin pumping, and two-magnon scattering (TMS) terms, a fuller understanding of the interplay among these terms and of how to suppress each term in an ultrathin ferromagnet is highly significant.

The magnetization damping was formulated phenomenologically as the Gilbert damping constant α by Gilbert [25] and has been studied both theoretically and experimentally for several decades [26–29]. In a ferromagnetic (FM)/nonmagnetic (NM) bilayer, the Gilbert damping constant can be decomposed into three terms as a function of the FM film thickness t_{FM}, as follows [30]:

$$\alpha = \alpha_{\mathrm{int}} + \alpha_{\mathrm{SP}} {t_{\mathrm{FM}}}^{-1} + \beta_{\mathrm{TMS}} {t_{\mathrm{FM}}}^{-2}, \qquad (1)$$

where α_{int}, α_{SP}, and β_{TMS} are the thickness-independent intrinsic damping constant of the FM layer, the damping constant due to spin pumping, and the TMS coefficient, respectively. The spin-pumping contribution α_{SP}, which emerges when the spin current from the FM layer relaxes in NM materials, was reported to be 0.055 nm for Co/Pt and 0.026 nm for Fe/Pt [31], and the TMS coefficient β_{TMS} was reported to be 2.73 ± 0.02 nm^2 for Co/SiO_2 and 0.41 ± 0.04 nm^2 for Co/Pt [32]. Because the contribution of TMS to magnon damping is proportional to the square of $1/t_{\mathrm{FM}}$, this contribution is greatly enhanced in nanometer-thick FMs, which then hampers the realization of low magnon damping in ultrathin FM films. Therefore, suppression of β_{TMS} is essential to the realization of low magnon damping in ultrathin FM films. β_{TMS} is also known to be dependent on the surface conditions of FM films, including the surface roughness and the surface magnetic anisotropy (SMA) [33,34]. Therefore, investigation of the correlation between the TMS-induced damping and the surface state of the FM film can also provide an invaluable guiding principle to aid in achieving low magnon damping in ultrathin FM films.

In this study, we investigate magnetization damping in ultrathin Co films equipped with a wide variety of NM seeding layers with different SMA energies, and then verify the significantly weak magnon damping that occurs in ultrathin Co by changing the seeding layer species. A scaling relationship between the TMS and the SMA is found that provides compelling evidence that the SMA governs the physics behind our findings. In addition to the photon relaxation rate and the magnon-photon coupling strength, the magnon relaxation rate of the ultrathin Co layer with the NM seeding layer is investigated quantitatively using a cavity quantum electrodynamics (QED) system, and potential approaches to realization of the strong coupling states are proposed.

II. Experiment

SiO_2 cap/MgO (2 nm)/Co (t_{Co})/NM (3 nm) film structures were prepared on SiO_2 substrates to investigate the correlation between TMS contribution and the uniaxial SMA field, where the Co

thickness t_{Co} ranged from 2 nm to 20 nm, and the NM materials were Ti, Cu, and Al, as shown in Fig. 1 and Table I. The Ti, Cu, Al, Co, and MgO layers were evaporated using electron beam deposition (EB-depo. in the table), where the deposition pressure was set to be 10^{-6} Pa. The SiO_2 cap and Ta seeding layers were deposited using radio frequency (RF) magnetron sputtering, where the base pressure was about 3×10^{-5} Pa. The Ar gas was used for the excitation of the plasma and the gas flow rate of Ar was 5 sccm, where the deposition pressure was 0.50 Pa. SiO_2 cap/MgO (2 nm)/Co (t_{Co}) films on SiO_2 substrates were also prepared for use as reference samples. To investigate the correlation between the TMS contributions and the uniaxial SMA field at the Co/NM interfaces, two dependences of the FMR signal, i.e., its microwave-frequency and magnetic-field-angular dependences, were investigated. The microwave-frequency dependence FMR signals was measured to estimate the Gilbert damping constant by the broadband FMR measurement using coplanar waveguide (CPW). With fixing the microwave frequency, the intensity of microwave transition was measured by sweeping the external magnetic field from 0 mT and 300 mT along the in-plane direction (see Fig. 2(a)). The similar measurements were consulted under different microwave frequencies and the microwave-frequency dependence of the FMR signals was measured, where the applied microwave frequency was varied from 5 to 15 GHz and the input power was set at 10 dBm. To measure the angle-dependent FMR spectra, the JES-FA200 electron spin resonance (ESR) spectrometer (JEOL Resonance Inc., Japan) was used, in which the TE_{011} mode was excited, and the microwave frequency and power at the output port were 9.12 GHz and 10 dBm, respectively.

The FMR measurement in a TiO_2 cavity with a high quality factor was performed by using a 2-nm-thick Co film on the Ta seeding layer to estimate the magnon relaxation rate, the photon relaxation rate, and the coupling strength. A Co (2 nm)/Ta (3 nm) film was deposited on a 1.0 mm × 0.8 mm SiO_2 substrate using RF magnetron sputtering. Single crystalline TiO_2 (rutile) has a high dielectric constant (ε~90) [35,36], and the cavity's quality factor was reported to be exceed 10^6 at low temperature [37], and that at the room temperature is about 10^4 (see Supplemental Materials A [38]).

The dimension of the rutile resonator in our experiments is Ø5.1 mm (outer) × Ø1.5 mm (inner) × 5.9 mm (height). The sample was set on an AlN-based ceramic rod and a microwave signal was applied from the VNA through the Cu loop coil into the rutile cavity, in which the excited mode was $TE_{01\delta}$. The microwave frequency was swept from 5.6 to 5.7 GHz, and the microwave power at the output port was −10 dBm. A magnetic field was then applied along the Co/Ta interface plane. The S_{11} parameter was measured, and the frequency and external magnetic field dependences of the S_{11} parameter were then estimated. All measurements were performed at room temperature.

III. Results and Discussion

Figure 2(b) shows the frequency dependence characteristics of the FMR signals from the 20-nm-thick Co sample with the Cu seeding layer. The frequency dependence of the half-width at half maximum (HWHM), designated ΔH, of the FMR spectra was estimated using the Lorentzian function [24,39] (see details in Supplemental Materials B [38]). The dependence of ΔH is known to be expressed using the following equation [39]: $\mu_0 \Delta H = 2\pi f \alpha/\gamma + \mu_0 \Delta H_0$, where f and $\mu_0 \Delta H_0$ represent the microwave frequency and the frequency-independent inhomogeneous linewidth, respectively. Here, the Gilbert damping constant can be extracted from the slope of the fitting function, $\mu_0 \Delta H = 2\pi f \alpha/\gamma + \mu_0 \Delta H_0$. The Gilbert damping constant α of this sample was estimated to be 0.026 ± 0.001, which is comparable to that of bulk Co [40]. The similar measurement was conducted to the samples of Co (10 nm)/SiO_2, Al, Cu and Ti, where the microwave frequency dependence of HWHM of these samples are shown in Fig. 2(c). The Gilbert damping constants of Co (10 nm)/SiO_2, Al, Cu and Ti were estimated to be 0.012 ± 0.001, 0.025 ± 0.001, 0.026 ± 0.002 and 0.018 ± 0.002, respectively. To investigate the dependence of the TMS coefficient on the nonmagnetic seeding layer species, the Gilbert damping constants of prepared samples with Ti, Cu, and Al seeding layers were estimated. Figure 2(d) shows the $1/t_{Co}$ dependences of the Gilbert damping constants of the samples with the different NM seeding layers; the corresponding dependence of a reference sample composed of a

single ultrathin Co film deposited on a SiO_2/Si substrate is also shown. The TMS coefficients of the ultrathin Co films with the Ti, Cu, Al, and SiO_2 seeding layers were 0.01 ± 0.07 nm^2, 0.35 ± 0.08 nm^2, 0.42 ± 0.05 nm^2, and 1.93 ± 0.20 nm^2, respectively, in the fitting performed using Eq. (1). Consequently, whereas the ultrathin Co films with Cu, Al, and SiO_2 seeding layers show large TMS contributions to the magnetization damping, the corresponding films with Ta and Ti seeding layers show substantial suppression of the TMS contribution. Note that these results are consistent with the previously reported result for realization of low magnon damping in nanometer-thick Co films through insertion of a Ta seeding layer [24,41], and more importantly, low magnon damping in ultrathin Co films can also be realized by inserting a Ti seeding layer. Our results indicate that the combination of FM and NM materials plays a crucial role in suppressing the TMS. Focusing on the ultrathin region, the Gilbert damping constants of the 2-nm-thick Co films with the Ti seeding layer is 0.020, which is approximately one-fifth of those for the 2-nm-thick Co films with the Cu and Al seeding layers (0.111 and 0.090, respectively) and comparable to 0.018 of the Co(20 nm)/Ti sample. Therefore, suppression of the TMS contribution by insertion of appropriate NM seeding layers leads to the occurrence of low magnon damping in nanometer-thick ferromagnetic films.

The β_{TMS} value is known to be proportional to the square of the SMA field, $h_{\mathrm{S_u}} = 2K_{\mathrm{S_u}}/M_{\mathrm{S}}$ [33,41], where $K_{\mathrm{S_u}}$ and M_{S} are the uniaxial magnetic anisotropy energy and the saturation magnetization, respectively. To understand the NM dependence of β_{TMS}, $h_{\mathrm{S_u}}$ is determined for each ultrathin-Co/NM interface by estimating the t_{Co} dependence of the uniaxial magnetic anisotropy field h_{u} while postulating that the diamagnetization of the Co remains unchanged within the film thickness region of interest in this study. The h_{u} of an FM material is dependent on $h_{\mathrm{S_u}}$ via the thickness of the FM film and can be described using the following equation:

$$h_{\mathrm{u}} = h_{\mathrm{V_u}} + h_{\mathrm{S_u}} t_{\mathrm{Co}}{}^{-1}, \qquad (2)$$

where $h_{\mathrm{V_u}}$ is the uniaxial magnetic anisotropy field of a bulk ferromagnet. An established method to estimate the $h_{\mathrm{S_u}}$ of an FM material involves measurement of the angular dependence of the FMR

spectra, which then enables determination of the effective uniaxial magnetic anisotropy field h_{eff} ($= h_{\mathrm{u}} - 4\pi M_{\mathrm{S}}$). Given that the in-plane magnetization is realized within the ultrathin Co film, the FMR frequency is expressed using the following equations, including h_{eff} [42]:

$$\left(\frac{\omega}{\gamma}\right)^2 = [\mu_0 H_{\mathrm{res}} \cos(\Theta_H - \Theta) - h_{\mathrm{eff}} \cos 2\Theta][\mu_0 H_{\mathrm{res}} \cos(\Theta_H - \Theta) + h_{\mathrm{eff}} \sin^2 \Theta], \quad (3)$$

$$\mu_0 H_{\mathrm{res}} \sin(\Theta_H - \Theta) + \frac{h_{\mathrm{eff}}}{2} \sin 2\Theta = 0, \quad (4)$$

where $\omega = 2\pi f$ and $\mu_0 H_{\mathrm{res}}$ are the microwave angular frequency and the resonance magnetic field of the FMR signal, respectively. In addition, Θ_H and Θ are the angles of the external magnetic field and the saturation magnetization with respect to the film plane, respectively, as shown in Fig. 3(a). Θ_H was rotated from 0° to 180°. Figures 3(b) and 3(c) show the Θ_H-dependence of the FMR spectra for the sample with the Co (10 nm)/SiO_2 structure and the resonance fields of the Co (10 nm)/SiO_2 structure, respectively. Because the sample had in-plane magnetic anisotropy, the resonance field at θ_{H} = 0° was the lowest. The upshift in the resonance field as a function of θ_{H} also supported the in-plane anisotropy of the ultrathin Co film. By solving Eqs. (3) and (4) self-consistently via substitution of the measured resonance fields (see details in Supplemental Materials C [38]), the h_{eff} of Co (10, 5 and 3 nm)/SiO_2 samples were estimated to be -1.83×10^3 mT, -1.55×10^3 mT and -1.08×10^3 mT, respectively, which are comparable with that of the Co(100 nm)/SiO_2 sample [42]. We note that our estimation method is a mathematical method to find the optimal parameters satisfying Eqs. (3) and (4). The reason why this approach was introduced is that it is not easy to identify the FMR field of the Co because saturation magnetization fields of the Co under an application of perpendicular to the plane magnetic field are too high, resulting in difficulty in numerical fitting using Eqs. (3) and (4) (see also Supplemental Materials C [38]). Figure 3(d) shows the complete dataset for the $1/t_{\mathrm{Co}}$ dependence of h_{eff} for the samples with the different NM seeding layers, and the magnitudes of $h_{\mathrm{S_u}}$ were determined from the slope of the linear fitting line to be 0.87 ± 0.23 T·nm (Ti), 1.3 ± 0.4 T·nm (Cu), 1.4 ± 0.1 T·nm (Al), and 3.23 ± 0.01 T·nm (SiO_2). As mentioned earlier, β_{TMS} is proportional to the

square of h_{S_u} at the Co/NM interface, and the TMS contribution should thus be suppressed significantly as the uniaxial SMA field of the ultrathin Co film is reduced by insertion of the NM seeding layers. In the next paragraph, we confirm that the TMS can indeed be suppressed by controlling the SMA field.

As shown in Figs. 4(a) and 4(b), β_{TMS} is proportional to the square of h_{S_u}, i.e., $\beta_{TMS} = C_{MD}(h_{S_u})^2$, where C_{MD} is the quantity to be determined based on the roughness of the FM films (see Eq. (94) in Ref. [31]) [32,33]. C_{MD} was estimated to be 0.18 ± 0.02 T^{-2}. The surface energy density dependences of selected NMs on the values of both β_{TMS} and h_{S_u} are shown in Fig. 4(c) and 4(d), respectively, where the magnitude of the NM surface energy density was cited from Ref. [43]. The h_{S_u} value at the ultrathin Co/NM interface decreases when the surface energy density of the NM material increases (see Fig. 4(c)), which is in good agreement with the results shown in Ref. [43]. Figure 4(d) shows the relationship between β_{TMS} and the surface energy density of the NM materials, where β_{TMS} also decreases as the surface energy density of the NM materials increases. Therefore, we have successfully substantiated the efficient suppression of the TMS of an ultrathin FM material by tuning its SMA through selection of appropriate NM seeding layers. This result indicates that the uniaxial SMA is dependent on the selection of the NM seeding layer located below the ultrathin Co film, which plays a significant role in the determination of the TMS contribution to magnon damping in ultrathin Co films. The noteworthy is that the β_{TMS} and h_{S_u} of the sample with SiO_2/Co/Ta is also strongly suppressed, and in fact, the lowest among all of measured samples (see Supplemental Materials D [38]) because the Ta has significantly high surface energy density and allows growth of Co with good crystallography, which is consistent with the realization of low magnon damping in 1-nm Co film on Ta seeding layer [24]. Albeit direct comparison of the results on the SiO_2/Co/Ta with those on the other samples fabricated by EB deposition was not conducted because the SiO_2/Co/Ta was fabricated by sputtering (see Table I), the SiO_2/Co/Ta sample is suitable for the following coupling measurements because of its quite low β_{TMS}. Thus, the coupling measurements of the

sample of SiO_2/Co(2 nm)/Ta using a rutile resonator was conducted, which is described in the next paragraph.

As a first step toward realization of magnon-photon strong coupling using ultrathin FM films, measurements to estimate the coupling strengths of magnons and photons in addition to their damping were conducted in an ultrathin Co film on a Ta seeding layer using the rutile resonator with the high-quality factor. The full width at half-maximum, κ_i, represents the microwave photon relaxation rate in the rutile resonator, which was extracted by fitting the microwave frequency dependence of the input reflection coefficient of the scattering parameter S_{11} at each external magnetic field as shown in Fig. 5(b) where the data is obtained by subtracting linear and weak background signals from the raw data (see Supplemental Materials E [38]). The fitting function is expressed as following equation:

$$S_{11} = \frac{i(\omega - \omega_{\mathrm{c}}\ ) + \frac{\kappa_{\mathrm{e}} - \kappa_{\mathrm{i}}}{2}}{i(\omega - \omega_{\mathrm{c}}\ ) - \frac{\kappa_{\mathrm{e}} + \kappa_{\mathrm{i}}}{2}}, \qquad (5)$$

where ω_{c} and κ_{e} are the resonance angular frequency of the rutile resonator and the relaxation rate of microwave photons passing through a coaxial cable connected to the coil, respectively. Figure 5(c) shows κ_i as a function of the external magnetic field, and a clear resonance peak was observed successfully, even from the 2-nm-thick Co film. In input-output theory [44,45], κ_i is expressed using the following equation (see also the Appendix for a more detailed description):

$$\kappa_i = \kappa_{\mathrm{i0}} + \gamma_{\mathrm{m}} \frac{{g_{\mathrm{eff}}}^2}{(\omega - \omega_{\mathrm{b}})^2 + \left(\frac{\gamma_{\mathrm{m}}}{2}\right)^2}, \qquad (6)$$

$$\omega_{\mathrm{b}} = \gamma\sqrt{\mu_0 H(\mu_0 H + M_{\mathrm{eff}})}, \qquad (7)$$

where κ_{i0}, γ_{m}, and ω_{b} are the linewidth without FMR excitation, the relaxation rate of an excited magnon, and the FMR angular frequency with in-plane magnetization, respectively. The relaxation rate corresponds to the linewidth of the magnetostatic mode. The red broken line shown in Fig. 5(c) depicts the fitting result obtained using Eq. (6), where $\kappa_{\mathrm{i0}} = 2\pi \times 22.7$ MHz, $g_{\mathrm{eff}} = 2\pi \times 3.88$ MHz, and $\gamma_{\mathrm{m}} = 2\pi \times 745$ MHz. In addition, M_{eff} was estimated to be 0.792 T, which is comparable to the magnitude of the effective magnetization in an ultrathin Co film [23]. The photon decay rate in the

rutile resonator with the sample was enhanced by a factor of 20 compared with the rate without the sample (2π × 1 MHz), which is most likely attributed to microwave absorption occurring in the metallic sample (see Supplemental Materials A [38]).

The coupling strength between the single spin and the photon mode can be expressed as $g_{0,\mathrm{Co}} = g^*_{\mathrm{Co}}\mu_{\mathrm{B}}B_{\mathrm{zpf}}/\sqrt{2}\hbar$ (see the derivation in Appendix B), where g^*_{Co} and B_{zpf} are the g-factor of Co and the vacuum fluctuation of the microwave magnetic field in the rutile resonator when applied to the single spin in the Co atom. B_{zpf} was estimated to be 5.4 pT, and $g_{0,\mathrm{Co}}$ was calculated to be 2π × 133 mHz in a COMSOL simulation. Since the effective coupling strength is expressed as $g_{\mathrm{eff}} = g_{0,\mathrm{Co}}\sqrt{N}$ [3] and the number of spins in a 2-nm-thick Co film is calculated to be 6.192×10^{14}, the estimated effective coupling strength of the 2-nm-thick Co film in the rutile resonator was estimated to be 2π × 3.31 MHz. The magnon-photon coupling state of rutile resonator and Co (2 nm)/Ta system is weak, since the estimated parameters g_{eff}, γ_{m} and κ_{i0} fulfills the following relation, $g_{\mathrm{eff}} < \gamma_{\mathrm{m}}, \kappa_{\mathrm{i0}}$. Fig. 5(d) shows a color map of the $|S_{11}|$ parameter, and indeed, the magnon-photon hybrid system is in a weak coupling regime. Meanwhile, the notable is the photon mode linewidth was slightly increased at around the external magnetic field, where a magnon is excited (see Fig. 5(c)). Therefore, the microwave photon and the excited magnon can interact with each other, yielding an additional decay path for the photon mode. Although estimation of coupling parameters in a weakly coupled regime in ultrathin metallic films has not been so far easy, our approach enables quantitively estimating the parameters of such ultrathin films by measuring the additional decay rate in the 3D resonator with high-quality factor, which is significance of this study.

Although it has been realized to provide tunability for the strong magnon-photon coupling system based on $Ye_3Fe_5O_{12}$ (YIG) by controlling microwave power [14,15], to control the magnon-photon coupling state via electric modulation of magnon is still a significant challenge, since its realization expands a border of an application of quantum coupling systems by means of conventional electronic approaches, such as that for field-effect transistors. Hence, magnon-photon

coupling between magnons excited in ultrathin FM films and microwave photons can pave the way toward realization of a gate-tunable magnon-photon coupling system. To realize a gate-tunable strong coupling regime using ultrathin FMs, weaker and tunable magnon damping enabling tunable coupling strength is required. The TMS contribution in such an ultrathin FM film can be excluded successfully by inserting Ta or Ti layers with small SMA fields. In contrast, the intrinsic contribution α_{int} of Co is still not small enough (~2.0×10^{-2}) to realize strong magnon-photon coupling because of the electron-magnon damping in the Co. Therefore, one possible approach to circumvent this problem may be to use a ferromagnetic metal that suppresses the electron-magnon damping, e.g., $Co_{25}Fe_{75}$ [28], because the α of this metal is 2.1×10^{-3}. The other potential approach is to introduce a superconducting inductor-capacitor (LC) circuit. In fact, although the α value of $Ni_{81}Fe_{19}$ (Py) is 2.2×10^{-2}, which is comparable to the damping constant of the ultrathin-Co/Ti sample, strong magnon-photon coupling was realized using the superconducting LC circuit [13,46]. Combination of the above approaches enables strong magnon-photon coupling that is gate-tunable to be realized.

IV. Conclusion

The TMS phenomenon in ultrathin Co that hampers efficient magnon excitation was examined in this study to allow the large magnon relaxation that impedes possible strong coupling of magnons and photons to be suppressed. We demonstrated successfully that the TMS in ultrathin Co films can be suppressed greatly by reducing the SMA field of the Co layer through insertion of Ta or Ti seeding layers. We also revealed the correlation between TMS in ultrathin Co and the surface energy density of the NM seeding layers below the ultrathin Co layer. These findings illustrate the importance of selecting appropriate NM seeding layers for efficient suppression of TMS and can provide a guiding principle to enable realization of low-magnon damping in ultrathin FM films, where the magnetization and magnon excitation are gate-tunable. In view of the quantum technologies that use magnon-photon

coupling, this study can pave the way toward realization of tunable magnon and photon coupling states by introducing weaker intrinsic magnon damping materials and systems to allow efficient coupling.

Appendix A. Derivation of the photon mode linewidth with the coupling FMR mode

In input-output theory [44], the operators that express the magnon mode, denoted by a, and the resonator mode, denoted by b, which couple with each other, are given by:

$$\frac{da}{dt} = -i\omega_c a - \frac{\kappa_{i0} + \kappa_e}{2} a - igb - \sqrt{\kappa_e} a_{in}, \quad \text{(A1)}$$

$$\frac{db}{dt} = -i\omega_b b - \frac{\gamma_m}{2} b - iga, \quad \text{(A2)}$$

where ω_c and ω_b are the microwave angular frequency and the magnon angular frequency, respectively. In addition, g, γ_m, κ_{i0}, κ_e, and a_{in} denote the coupling coefficient of the magnon mode and the resonator mode, the magnon damping coefficient, the microwave photon damping coefficient, the decay to the transmission line, and the input operators for the microwave signal, respectively. The operator expression rotating with angular frequencies, $a = \tilde{a}e^{-i\omega t}$ and $b = \tilde{b}e^{-i\omega_b t}$, are substituted into Eqs. (A1) and (A2),

$$\left[-i(\omega - \omega_c) + \frac{\kappa_{i0} + \kappa_e}{2}\right] \tilde{a} = -ig\tilde{b} - \sqrt{\kappa_e}\tilde{a}_{in}, \quad \text{(A3)}$$

$$\left[-i(\omega - \omega_b) + \frac{\gamma_m}{2}\right] \tilde{b} = -ig\tilde{a}. \quad \text{(A4)}$$

We solve Eq. (A4) for $\tilde{b}$ and substitute the result into (A3), which gives us the equation for the microwave input operator and the operator of the resonator mode. By defining the susceptibility as χ, the result can be calculated using the following equation:

$$\chi\tilde{a} = -\sqrt{\kappa_e}\tilde{a}_{in}, \quad \text{(A5)}$$

$$\chi = \left[-i(\omega - \omega_c) + \frac{\kappa_{i0} + \kappa_e}{2} + \frac{g^2}{-i(\omega - \omega_b) + \frac{\gamma_m}{2}}\right], \quad \text{(A6)}$$

Around $\omega = \omega_c$, the real part of χ represents the HWHM of $|S_{11}|$, and then the damping coefficient of the resonator mode coupled with the magnon mode can be expressed as κ_i:

$$\kappa_i = 2\mathrm{Re}(\chi) = \kappa_{i0} + \gamma_m \frac{g^2}{(\omega_c - \omega_b)^2 + (\frac{\gamma_m}{2})^2}. \quad \text{(A7)}$$

Appendix B. Derivation of coupling strength between single spin in ferromagnet and photon mode

The Hamiltonian of the magnon-photon interaction is expressed as the following product of magnetic z-component $\hat{B}_z$ due to the microwave exciting photon mode $TE_{01\delta}$ in the resonator and the z-component of the magnetic moment $\hat{\mu}_z$ in ferromagnet,

$$H = \hat{B}_z \hat{\mu}_z. \qquad \text{(B1)}$$

Here, the z direction is defined along the direction of the ac magnetic field. The ac magnetic field generated by the microwave in the resonator is represented as the following equation,

$$\hat{B}_z = B_{\text{zpf}}(\hat{a} + \hat{a}^\dagger), \qquad \text{(B2)}$$

where the B_{zpf}, $\hat{a}$ and $\hat{a}^\dagger$ are zero-point fluctuation of magnetic field in the resonator, creation, and annihilation operators of photon, respectively.

The magnetic moment in the ferromagnet is expressed as the summation of the contribution of each magnetic spin, $\hat{S}_i$, as ~~shown~~ in the following equation, $\hat{\mu}_x = g\mu_B \sum \hat{S}_i$. Each magnetic spin operator of $\hat{S}_i$ in ferromagnet is expressed by the Holstein-Primakoff transformation as follows,

$$\hat{S}_i^+ = \sqrt{2S}\left(1 - \frac{\hat{b}_i^\dagger \hat{b}_i}{2S}\right)^{\frac{1}{2}} \hat{b}_i, \qquad \text{(B3)}$$

$$\hat{b}_i = \frac{1}{\sqrt{N}} \sum_{\boldsymbol{k}} e^{-i\boldsymbol{k}\cdot\boldsymbol{R}_i}\, \hat{b}_{\boldsymbol{k}}, \qquad \text{(B4)}$$

where $\hat{b}_i$ and $\hat{b}_{\boldsymbol{k}}$ are bosonic operators expressing magnon excitation in the real space and in the wavevector space, respectively. The S and N are the number of spins in each atom and that of atoms in the ferromagnet, respectively. The excitation numbers of magnon, $\hat{b}_k^\dagger \hat{b}_k$, are assumed to be sufficiently small and the first order of $\hat{b}_{\boldsymbol{k}}$ is remained in Eq. (B3). In addition, since only the $\boldsymbol{k} = 0$ magnon mode is excited with uniform ac magnetic field, Eq. (B3) reduces to the following equation,

$$\hat{S}_i^+ = \sqrt{2S/N}\ \hat{b}. \qquad \text{(B5)}$$

Here, the magnon mode at the $\boldsymbol{k} = 0$, $\hat{b}_{\boldsymbol{0}}$, is defined to be the $\hat{b}$ and each magnetic spin operator is considered to be the same. Thus, the magnetic moment of the $\boldsymbol{k} = 0$ magnon mode, $\hat{\mu}_x$, is written as,

$$\hat{\mu}_x = g\mu_B N\hat{S}_{ix}$$

$$= \frac{g\mu_B N}{2}\left(\hat{S}_i^+ + \hat{S}_i^-\right)$$

$$= \frac{g\mu_B}{2}\sqrt{\frac{NS}{2}}\left(\hat{b} + \hat{b}^\dagger\right). \qquad \text{(B6)}$$

Finally, Eqs. (B2) and (B6) were substituted into Eq. (B1) and the magnon-photon coupling Hamiltonian was obtained by applying the rotating wave approximation,

$$\widehat{H} = \frac{g\mu_B B_{\text{zpf}}}{\sqrt{2}}\sqrt{NS}\left(\hat{a}^\dagger\hat{b} + \hat{a}\hat{b}^\dagger\right) = \hbar g_{0,\text{Co}}\sqrt{NS}\left(\hat{a}^\dagger\hat{b} + \hat{a}\hat{b}^\dagger\right), \qquad \text{(B7)}$$

where $g_{0,\text{Co}}$ is defined as the coupling strength between single spin in ferromagnet and photon mode and described as,

$$g_{0,\text{Co}} = \frac{g\mu_B B_{\text{zpf}}}{\sqrt{2}\hbar}. \qquad \text{(B8)}$$

Acknowledgement

This work was supported in part by the Japan Society for the Promotion of Science (JSPS) Research Fellow Program (grant no. 22J21232), JSPS KAKENHI (grant no. 19H05602), the JST ERATO project (grant no. JPMJER1601), and the Spintronics Research Network of Japan (Spin-RNJ). K. K. and K. U. acknowledge Dr. K. Matsuura and Prof. Y. Nakamura for productive interactions.

References

[1] A. V. Chumak, A. A. Serga, and B. Hillebrands, *Magnon Transistor for All-Magnon Data Processing*, Nat. Commun. **5**, 4700 (2014).

[2] K. S. Das, F. Feringa, M. Middelkamp, B. J. van Wees, and I. J. Vera-Marun, *Modulation of Magnon Spin Transport in a Magnetic Gate Transistor*, Phys. Rev. B **101**, 054436 (2020).

[3] H. Huebl, C. W. Zollitsch, J. Lotze, F. Hocke, M. Greifenstein, A. Marx, R. Gross, and S. T. B. Goennenwein, *High Cooperativity in Coupled Microwave Resonator Ferrimagnetic Insulator Hybrids*, Phys. Rev. Lett. **111**, 127003 (2013).

[4] X. Zhang, C.-L. Zou, L. Jiang, and H. X. Tang, *Strongly Coupled Magnons and Cavity Microwave Photons*, Phys. Rev. Lett. **113**, 156401 (2014).

[5] Y. Tabuchi, S. Ishino, T. Ishikawa, R. Yamazaki, K. Usami, and Y. Nakamura, *Hybridizing Ferromagnetic Magnons and Microwave Photons in the Quantum Limit*, Phys. Rev. Lett. **113**, 083603 (2014).

[6] Y. Nakamura, Y. A. Pashkin, and J. S. Tsai, *Coherent Control of Macroscopic Quantum States in a Single-Cooper-Pair Box*, Nature **398**, 786 (1999).

[7] X. Zhang, C.-L. Zou, N. Zhu, F. Marquardt, L. Jiang, and H. X. Tang, *Magnon Dark Modes and Gradient Memory*, Nat. Commun. **6**, 8914 (2015).

[8] M. Elyasi, Y. M. Blanter, and G. E. W. Bauer, *Resources of Nonlinear Cavity Magnonics for Quantum Information*, Phys. Rev. B **101**, 054402 (2020).

[9] Y. Tabuchi, S. Ishino, A. Noguchi, T. Ishikawa, R. Yamazaki, K. Usami, and Y. Nakamura, *Coherent Coupling between a Ferromagnetic Magnon and a Superconducting Qubit*, Science (80-.). **349**, 405 (2015).

[10] S. P. Wolski, D. Lachance-Quirion, Y. Tabuchi, S. Kono, A. Noguchi, K. Usami, and Y. Nakamura, *Dissipation-Based Quantum Sensing of Magnons with a Superconducting Qubit*, Phys. Rev. Lett. **125**, 117701 (2020).

[11] D. Lachance-Quirion, S. P. Wolski, Y. Tabuchi, S. Kono, K. Usami, and Y. Nakamura, *Entanglement-Based Single-Shot Detection of a Single Magnon with a Superconducting Qubit*, Science (80-.). **367**, 425 (2020).

[12] H. Maier-Flaig, M. Harder, R. Gross, H. Huebl, and S. T. B. Goennenwein, *Spin Pumping in Strongly Coupled Magnon-Photon Systems*, Phys. Rev. B **94**, 054433 (2016).

[13] J. T. Hou and L. Liu, *Strong Coupling between Microwave Photons and Nanomagnet Magnons*, Phys. Rev. Lett. **123**, 107702 (2019).

[14] O. Lee, K. Yamamoto, M. Umeda, C. W. Zollitsch, M. Elyasi, T. Kikkawa, E. Saitoh, G. E. W. Bauer, and H. Kurebayashi, *Nonlinear Magnon Polaritons*, ArXiv: **2011**, 10889v1 (2022).

[15] J. Xu, C. Zhong, X. Han, D. Jin, L. Jiang, and X. Zhang, *Coherent Gate Operations in Hybrid Magnonics*, Phys. Rev. Lett. **126**, 207202 (2021).

[16] H. Maier-Flaig, M. Harder, S. Klingler, Z. Qiu, E. Saitoh, M. Weiler, S. Geprägs, R. Gross, S. T. B. Goennenwein, and H. Huebl, *Tunable Magnon-Photon Coupling in a Compensating Ferrimagnet—from Weak to Strong Coupling*, Appl. Phys. Lett. **110**, 132401 (2017).

[17] K. Shimamura, D. Chiba, S. Ono, S. Fukami, N. Ishiwata, M. Kawaguchi, K. Kobayashi, and T. Ono, *Electrical Control of Curie Temperature in Cobalt Using an Ionic Liquid Film*, Appl. Phys. Lett. **100**, 122402 (2012).

[18] D. Chiba and T. Ono, *Control of Magnetism in Co by an Electric Field*, J. Phys. D. Appl. Phys. **46**, 213001 (2013).

[19] T. Maruyama, Y. Shiota, T. Nozaki, K. Ohta, N. Toda, M. Mizuguchi, A. A. Tulapurkar, T. Shinjo, M. Shiraishi, S. Mizukami, Y. Ando, and Y. Suzuki, *Large Voltage-Induced Magnetic Anisotropy Change in a Few Atomic Layers of Iron*, Nat. Nanotechnol. **4**, 158 (2009).

[20] S. Dushenko, M. Hokazono, K. Nakamura, Y. Ando, T. Shinjo, and M. Shiraishi, *Tunable Inverse Spin Hall Effect in Nanometer-Thick Platinum Films by Ionic Gating*, Nat. Commun. **9**, 3118 (2018).

[21] S.-I. Yoshitake, R. Ohshima, T. Shinjo, Y. Ando, and M. Shiraishi, *Modulation of Spin Conversion in a 1.5 Nm-Thick Pd Film by Ionic Gating*, Appl. Phys. Lett. **117**, 092406 (2020).

[22] R. Ohshima, Y. Kohsaka, Y. Ando, T. Shinjo, and M. Shiraishi, *Modulation of Spin-Torque Ferromagnetic Resonance with a Nanometer-Thick Platinum by Ionic Gating*, Sci. Rep. **11**, 21779 (2021).

[23] B. Heinrich, J. F. Cochran, M. Kowalewski, J. Kirschner, Z. Celinski, A. S. Arrott, and K. Myrtle, *Magnetic Anisotropies and Exchange Coupling in Ultrathin Fcc Co(001) Structures*, Phys. Rev. B **44**, 9348 (1991).

[24] S. Yoshii, R. Ohshima, Y. Ando, T. Shinjo, and M. Shiraishi, *Detection of Ferromagnetic Resonance from 1 Nm-Thick Co*, Sci. Rep. **10**, 15764 (2020).

[25] T. L. Gilbert, *Classics in Magnetics A Phenomenological Theory of Damping in Ferromagnetic Materials*, IEEE Trans. Magn. **40**, 3443 (2004).

[26] Y. Tserkovnyak, A. Brataas, and G. E. W. Bauer, *Enhanced Gilbert Damping in Thin Ferromagnetic Films*, Phys. Rev. Lett. **88**, 117601 (2002).

[27] L. Liu, T. Moriyama, D. C. Ralph, and R. A. Buhrman, *Spin-Torque Ferromagnetic Resonance Induced by the Spin Hall Effect*, Phys. Rev. Lett. **106**, 036601 (2011).

[28] M. A. W. Schoen, D. Thonig, M. L. Schneider, T. J. Silva, H. T. Nembach, O. Eriksson, O. Karis, and J. M. Shaw, *Ultra-Low Magnetic Damping of a Metallic Ferromagnet*, Nat. Phys. **12**, 839 (2016).

[29] H. Hayashi, A. Musha, H. Sakimura, and K. Ando, *Spin-Orbit Torques Originating from the Bulk and Interface in Pt-Based Structures*, Phys. Rev. Res. **3**, 013042 (2021).

[30] L. Zhu, D. C. Ralph, and R. A. Buhrman, *Effective Spin-Mixing Conductance of Heavy-Metal–Ferromagnet Interfaces*, Phys. Rev. Lett. **123**, 057203 (2019).

[31] A. Conca, S. Keller, L. Mihalceanu, T. Kehagias, G. P. Dimitrakopulos, B. Hillebrands, and E. T. Papaioannou, *Study of Fully Epitaxial Fe/Pt Bilayers for Spin Pumping by Ferromagnetic*

Resonance Spectroscopy, Phys. Rev. B **93**, 134405 (2016).

[32] L. Zhu, L. Zhu, D. C. Ralph, and R. A. Buhrman, *Origin of Strong Two-Magnon Scattering in Heavy-Metal/Ferromagnet/Oxide Heterostructures*, Phys. Rev. Appl. **13**, 034038 (2020).

[33] R. Arias and D. L. Mills, *Extrinsic Contributions to the Ferromagnetic Resonance Response of Ultrathin Films*, Phys. Rev. B **60**, 7395 (1999).

[34] A. Azevedo, a. B. Oliveira, F. M. de Aguiar, and S. M. Rezende, *Extrinsic Contributions to Spin-Wave Damping and Renormalization in Thin Ni50Fe50 Films*, Phys. Rev. B **62**, 5331 (2000).

[35] M. E. Tobar, J. Krupka, E. N. Ivanov, and R. A. Woode, *Anisotropic Complex Permittivity Measurements of Mono-Crystalline Rutile between 10 and 300 K*, J. Appl. Phys. **83**, 1604 (1998).

[36] W. A. Huttema, B. Morgan, P. J. Turner, W. N. Hardy, X. Zhou, D. A. Bonn, R. Liang, and D. M. Broun, *Apparatus for High-Resolution Microwave Spectroscopy in Strong Magnetic Fields*, Rev. Sci. Instrum. **77**, 023901 (2006).

[37] K. Hashimoto, K. Cho, T. Shibauchi, S. Kasahara, Y. Mizukami, R. Katsumata, Y. Tsuruhara, T. Terashima, H. Ikeda, M. A. Tanatar, H. Kitano, N. Salovich, R. W. Giannetta, P. Walmsley, A. Carrington, R. Prozorov, and Y. Matsuda, *A Sharp Peak of the Zero-Temperature Penetration Depth at Optimal Composition in BaFe 2 (As 1– x P x) 2*, Science (80-.). **336**, 1554 (2012).

[38] See Supplemental Materials at (url) ,which contains absorption curve of empty rutile resonator at room temperature ,the estimation method of the Gilbert damping constant by frequency dependence of broadband ferromagnetic resonance,the evaluation of estimated effective uniaxial magnetic anisotropy, correlation between TMS contribution and SMA field of samples with Co/SiO_2, Raw data of S_{11} parameter for the rutile resonator with the Co(2 nm)/Ta sample and Simulation of the amplitude of ac magnetic field excited in rutile resonator.

[39] R. Ohshima, S. Klingler, S. Dushenko, Y. Ando, M. Weiler, H. Huebl, T. Shinjo, S. T. B.

Goennenwein, and M. Shiraishi, *Spin Injection into Silicon Detected by Broadband Ferromagnetic Resonance Spectroscopy,* Appl. Phys. Lett. **110**, 182402 (2017).

[40] S. Trudel, O. Gaier, J. Hamrle, and B. Hillebrands, *Magnetic Anisotropy, Exchange and Damping in Cobalt-Based Full-Heusler Compounds: An Experimental Review*, J. Phys. D. Appl. Phys. **43**, 193001 (2010).

[41] L. Zhu, D. C. Ralph, and R. A. Buhrman, *Spin-Orbit Torques in Heavy-Metal–Ferromagnet Bilayers with Varying Strengths of Interfacial Spin-Orbit Coupling*, Phys. Rev. Lett. **122**, 077201 (2019).

[42] O. Kohmoto, S. Araki, and C. Alexander, *Characterization of Damaged Layer Using AC Surface Photovoltagein Silicon Wafers*, Jpn. J. Appl. Phys. **32**, 3962 (1993).

[43] A. J. Lee, A. S. Ahmed, B. A. McCullian, S. Guo, M. Zhu, S. Yu, P. M. Woodward, J. Hwang, P. C. Hammel, and F. Yang, *Interfacial Rashba-Effect-Induced Anisotropy in Nonmagnetic-Material-Ferrimagnetic-Insulator Bilayers*, Phys. Rev. Lett. **124**, 257202 (2020).

[44] A. A. Clerk, M. H. Devoret, S. M. Girvin, F. Marquardt, and R. J. Schoelkopf, *Introduction to Quantum Noise, Measurement, and Amplification*, Rev. Mod. Phys. **82**, 1155 (2010).

[45] D. T. Gillespie, *The Mathematics of Brownian Motion and Johnson Noise*, Am. J. Phys. **64**, 225 (1996).

[46] Y. Li, T. Polakovic, Y.-L. Wang, J. Xu, S. Lendinez, Z. Zhang, J. Ding, T. Khaire, H. Saglam, R. Divan, J. Pearson, W.-K. Kwok, Z. Xiao, V. Novosad, A. Hoffmann, and W. Zhang, *Strong Coupling between Magnons and Microwave Photons in On-Chip Ferromagnet-Superconductor Thin-Film Devices*, Phys. Rev. Lett. **123**, 107701 (2019).

Table captions

Table I. List of the prepared samples and their preparation methods.

Sample #	Stacking order	Preparation method
1	SiO_2 cap / MgO (2) / Co (t_{Co}) / Ti (3) / SiO_2 sub	SiO_2 cap : Sputter MgO / Co / NM : EB-depo
2	SiO_2 cap / MgO (2) / Co (t_{Co}) / Al (3) / SiO_2 sub	
3	SiO_2 cap / MgO (2) / Co (t_{Co}) / Cu (3) / SiO_2 sub	
4	SiO_2 cap / MgO (2) / Co (t_{Co}) / SiO_2 sub	
5	SiO_2 cap / Co (2) / Ta (3) / SiO_2 sub	SiO_2/Co/Ta : Sputter

Table I. Yoshii *et al*.,

Figure captions

Figure 1. Schematics of the sample structures shown in Table I. The Co film thickness (t_{Co}) was varied from 2 nm to 20 nm. The samples were capped with a 2-nm-thick MgO layer and a 10-nm-thick SiO_2 layer for samples 1, 2, 3 and 4.

Figure 2. (a) Schematic of the experimental setting used in the CPW-FMR measurements. The external magnetic field was applied along the in-plane direction of the samples. (b) Frequency dependence of the FMR signals of Co (20 nm)/Cu, where the frequency was varied from 5 GHz to 15 GHz. (c) Frequency dependence of the HWHM in the Co (10 nm)/SiO_2, Al, Cu and Ti sample. (d) Co thickness dependence of the Gilbert damping constant α for the samples with the various NM seeding layers and the SiO_2 underlayer (i.e., the reference sample).

Figure 3. (a) Schematic of the measurement set-up used to determine the angular dependence of the FMR signals when using the ESR apparatus. (b) Angular dependence of the FMR signals of the Co (10 nm)/SiO_2 sample. (c) Angular dependence of the resonance fields of the Co (3, 5 and 10 nm)/SiO_2 samples. The broken red line represents the fitting line. (d) Co film thickness dependence of the uniaxial magnetic anisotropy field h_u, where closed lines represent the results obtained using the fitting function $h_u = h_{V_u} + h_{S_u} {t_{FM}}^{-1}$.

Figure 4. (a) Correlation diagram between the TMS coefficient β_{TMS} and the square of the SMA field $(h_{S_u})^2$. The broken line indicates the fitting result for the samples with the NM seeding layers. In the correlation between β_{TMS} and $(h_{S_u})^2$, the blue, red, green, and black points represent the data points for Co/Ti, Co/Cu, Co/Al, and Co/SiO_2, respectively. (b) The enlarged figure in the block broken square. Surface energy density dependence of the NM materials selected as the seeding layers on (c) β_{TMS} and (d) h_{S_u}, where the black broken lines in (c) and (d) show the values of the MgO/Co/SiO_2.

Figure 5. (a) Schematic of the measurement set-up used to perform the FMR measurements using the rutile cavity. The external magnetic field was applied in-plane along the sample and the microwave signal was applied via the coil. (b) Frequency dependence of $|S_{11}|$ at a zero external magnetic field, where the red line shows the fitting result obtained using Eq. (5). (c) External magnetic field dependence of κ_i, where the red broken line represents the fitting result obtained using Eq. (6). (d) Color map of $|S_{11}|$ for the external magnetic fields and microwave frequencies.

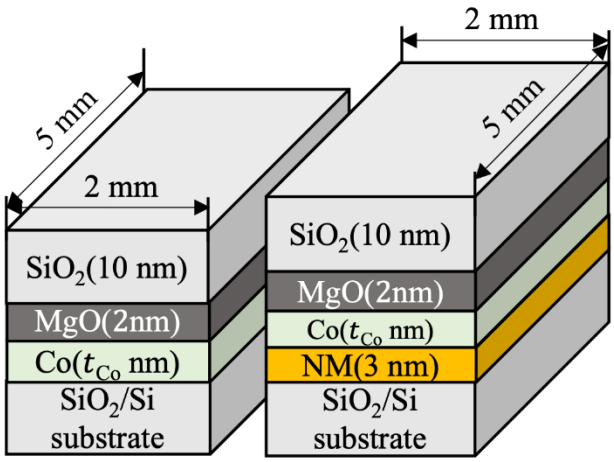

Fig. 1 Yoshii *et al*.

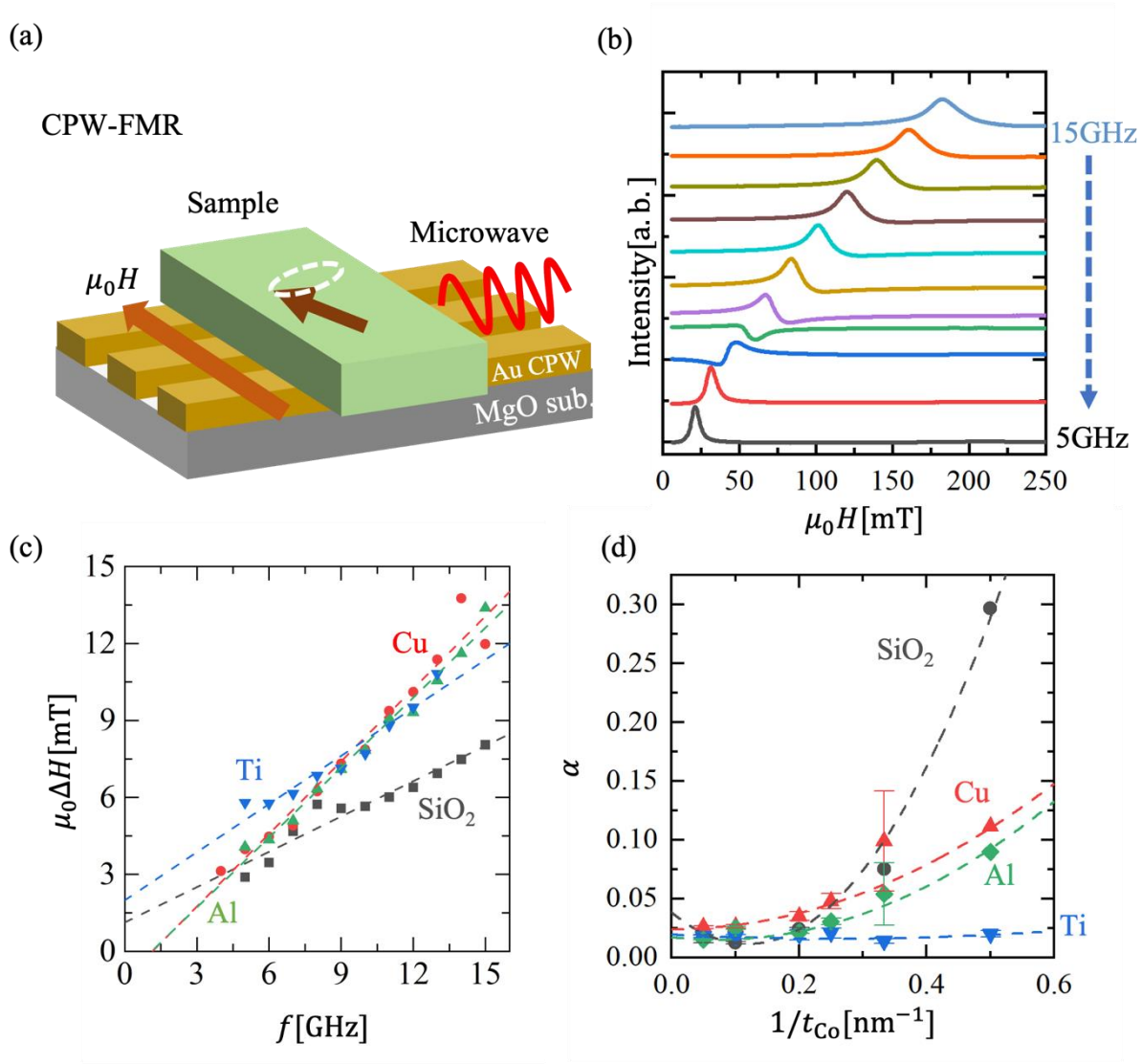

Fig. 2 Yoshii *et al.*

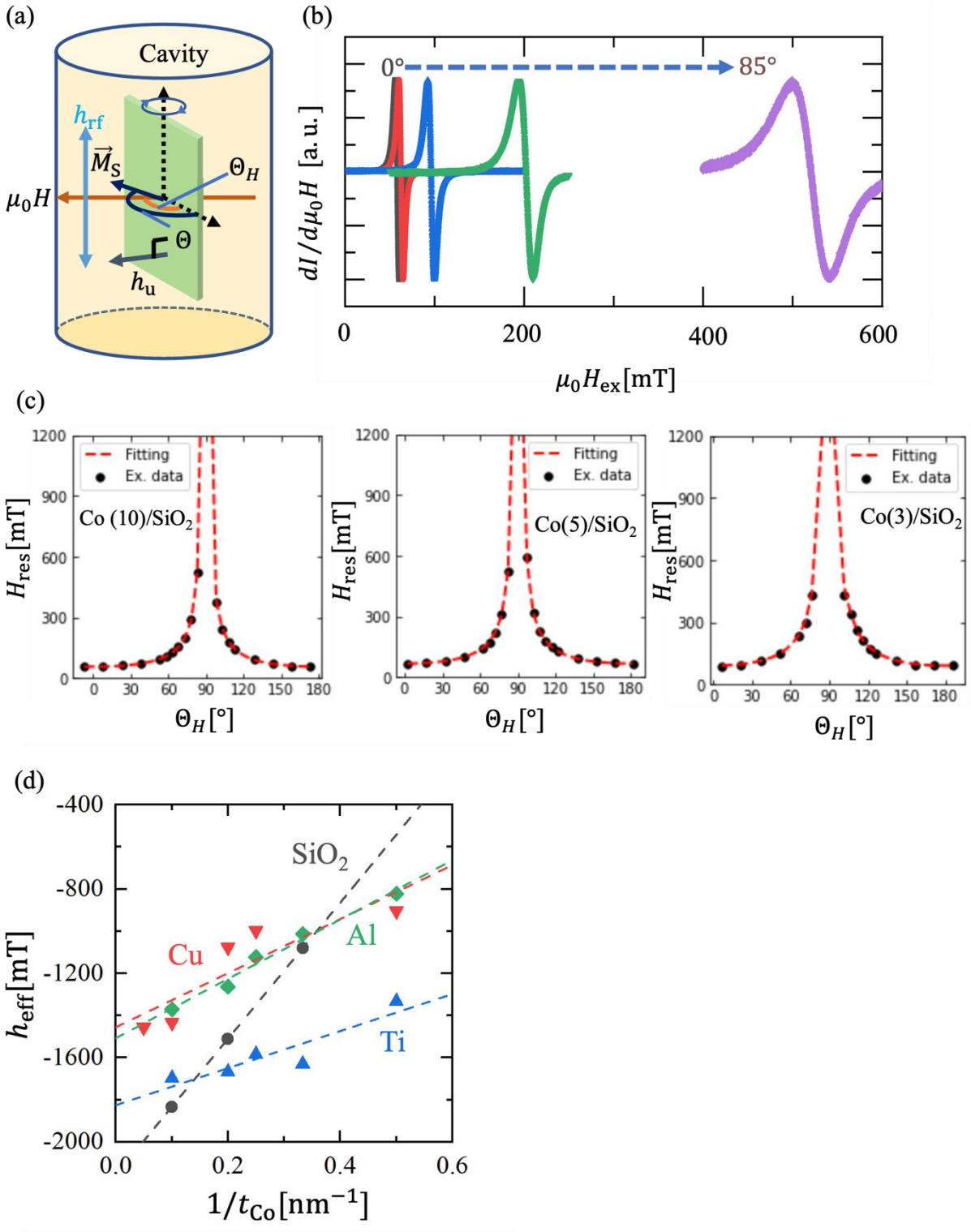

Fig. 3 Yoshii *et al.*

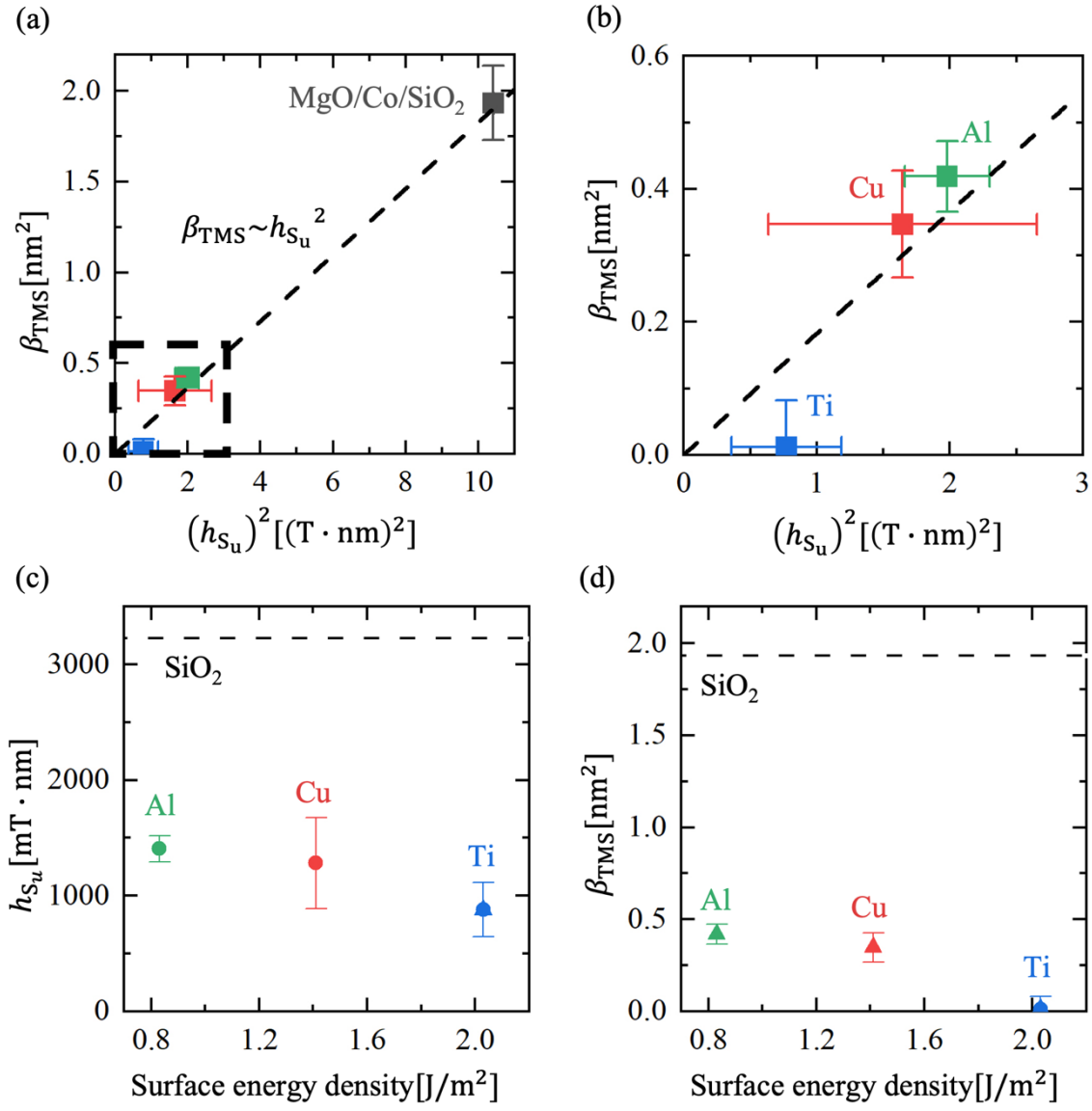

Fig. 4 Yoshii *et al.*

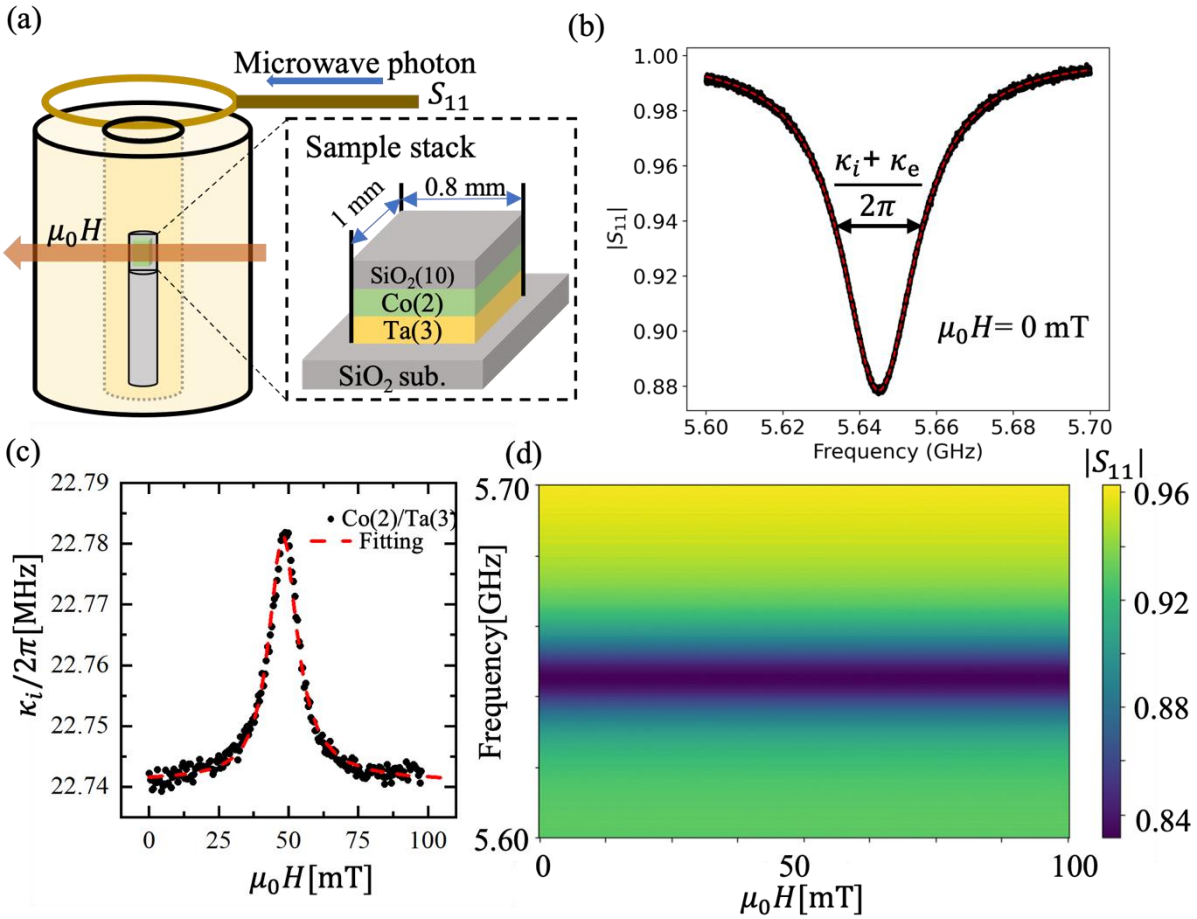

Fig. 5 Yoshii *et al.*